Gradual caldera collapse at Bárdarbunga volcano, Iceland, regulated by lateral magma outflow

Magnús T. Gudmundsson[1], Kristín Jónsdóttir[2], Andrew Hooper[3], Eoghan P. Holohan[4,5], Sæmundur A. Halldórsson[1], Benedikt G. Ófeigsson[2], Simone Cesca[4], Kristín S. Vogfjörd[2], Freysteinn Sigmundsson[1], Thórdís Högnadóttir[1], Páll Einarsson[1], Olgeir Sigmarsson[1,6], Alexander H. Jarosch[1], Kristján Jónasson[7], Eyjólfur Magnússon[1], Sigrún Hreinsdóttir[8], Marco Bagnardi[3], Michelle M. Parks[1], Vala Hjörleifsdóttir[9], Finnur Pálsson[1], Thomas R. Walter[4], Martin P.J. Schöpfer[10], Sebastian Heimann[4], Hannah I. Reynolds[1], Stéphanie Dumont[1], Eniko Bali[1], Gudmundur H. Gudfinnsson[1], Torsten Dahm[4], Matthew J. Roberts[2], Martin Hensch[2], Joaquín, M.C. Belart[1], Karsten Spaans[3], Sigurdur Jakobsson[1], Gunnar B. Gudmundsson[2], Hildur M. Fridriksdóttir[1,2], Vincent Drouin[1], Tobias Dürig[1], Guðfinna Adalgeirsdóttir[1], Morten S. Riishuus[1], Gro B.M. Pedersen[1], Tayo van Boeckel[1], Björn Oddsson[11], Melissa A. Pfeffer[2], Sara Barsotti[2], Baldur Bergsson[2], Amy Donovan[12], Mike R. Burton[13], Alessandro Aiuppa[14]

Accepted final proof of research article aaf898.
Published in Science 15 July 2016.

Cite this article as:
M. T. Gudmundsson et al., Science 353,aaf8988 (2016). DOI: 10.1126/science.aaf8988.

1: Nordvulk, Institute of Earth Sciences, University of Iceland, Sturlugata 7, 101 Reykjavík
2: Icelandic Meteorological Office, IS-150 Reykjavík, Iceland
3: Centre for the Observation and Modelling of Earthquakes, Volcanoes *and Tectonics (COMET), School of Earth and Environment, University of Leeds, Leeds LS2 9JT, UK*
4: GFZ German Research Centre for Geosciences, Telegrafenberg, 14473 Potsdam, Germany
5: UCD School of Earth Sciences, University College Dublin, Ireland
6: Laboratoire Magmas et Volcans, CNRS-Université Blaise Pascal-IRD, 63038 Clermont-Ferrand, France
7: Faculty of Industrial and Mechanical Engineering and Computer Science, University of Iceland, Hjarðarhagi 2-6, 107 Reykjavík, Iceland
8: GNS Science, PO Box 30368, Lower Hutt 5040, New Zealand
9: Departamento de Sismología, Instituto de Geofísica, Universidad Nacional Autónoma de Mexico, 04510 Ciudad de México, Mexico
10: Department for Geodynamics and Sedimentology, University of Vienna, Althanstrasse 14, A-1090 Vienna, Austria.
11: National Commissioner of the Icelandic Police, Department of Civil Protection and Emergency Management, Skúlagata 21, 101 Reykjavík, Iceland
12: King's College London, King's Building, Strand Campus, London WC2R 2LS, England, United Kingdom
13: University of Manchester, Williamson Building, Oxford Road, Manchester, M13 9PL, UK
14: University of Palermo – Piazza Marina, 61 90133, Palermo, Italy

Abstract

Large volcanic eruptions on Earth commonly occur with collapse of the roof of a crustal magma reservoir, forming a caldera. Only a few such collapses occur per century and lack of detailed observations has obscured insight into mechanical interplay between collapse and eruption. We use multi-parameter geophysical and geochemical data to show that the 110 km² and 65 m deep collapse of Bárdarbunga caldera in 2014-15 initiated through withdrawal of magma, and lateral migration through a 47 km long dyke, from a 12 km deep reservoir. Interaction between the pressure exerted by the subsiding reservoir roof and the physical properties of the subsurface flow path explain the gradual, near exponential decline of both collapse rate and the intensity of the 180-day- long eruption.

Calderas are 1 - 100 km diameter depressions found in volcanic regions of Earth and other planets. They mainly form by collapse of overburden into a subterranean magma reservoir during large volcanic eruptions, including the largest known super-eruptions (*1-8*). From 1900 to 2014 CE, only six cases have been documented and with varying degrees of detail. The collapses of Katmai in 1912 and Pinatubo in 1991 occurred during explosive silicic (andesite-rhyolite) eruptions, the largest of the 20th century. The collapses of Fernandina in 1968, Tolbachik in 1975-76, Miyakejima in 2000 and Piton de la Fournaise in 2007 were associated with mainly effusive mafic (basalt – basaltic andesite) intrusive activity and eruptions (*2*, *9-12*).

The consensus from field and modelling studies is that caldera collapse progresses from initial surface downsag to fault-controlled subsidence (*1*, *8*, *13*, *14*). The limited number of modern examples and the scarcity of geophysical data leaves open the question of whether collapse occurs suddenly or gradually during the course of an eruption. The issue of whether collapse drives magma movement and eruption or eruption drives collapse also remains unresolved. Previous geological, geophysical, and modeling studies have produced a diverse and inconsistent set of answers to such questions (*2*, *4*, *15*, *16*). The caldera collapse at Bárdarbunga in central Iceland from August 2014 to February 2015 offers a unique opportunity to address them directly.

The Bárdarbunga volcano and the Holuhraun eruption of 2014-15

Bárdarbunga volcano (Fig. 1) and its related fissure swarms form a 150 km long volcanic system on the boundary between the North-American and Eurasian tectonic plates. The volcano resides beneath the Vatnajökull ice cap and has a broadly elliptic 11 by 8 km wide and 500-700 m deep caldera with a long axis trending ENE. About 700-800 m of ice fills the caldera (*17*, *18*). Over 20 eruptions have occurred on the fissure swarms outside the caldera in the last 12 centuries, including three that produced 1-4 km³ of magma, but no eruptions are known within the caldera in this period. (*19*).

At 4 UTC on 16 August 2014, the onset of intense seismicity beneath the caldera marked the beginning of a major rifting event (*20*). The seismic activity was mostly located in the SE-corner of the caldera in the first few hours, but it soon began to propagate out of the caldera towards the SE (Fig. 2). After propagating to about 7 km from the caldera rim, fifteen hours after the onset of seismicity (~19 UTC), the moving earthquake cluster took a 90° turn and started migrating towards the NE. In the two weeks that followed, surface deformation and migration of seismicity indicated that a magmatic dike propagated laterally northeastward for 41 km in the uppermost 6-10 km of the Earth's crust (*20*, *21*). On 31 August, a major effusive eruption began above the far end of the dike; this lasted six months and produced 1.5±0.2 km^3 of lava (~1.4±0.2 km^3 of bubble-free magma) (*22*), making it the largest in Iceland (or Europe) since the 1783-84 Laki eruption. Combined with the 0.5±0.1 km^3 dyke (*20*), the total volume of identified intruded and erupted magma was 1.9±0.3 km^3.

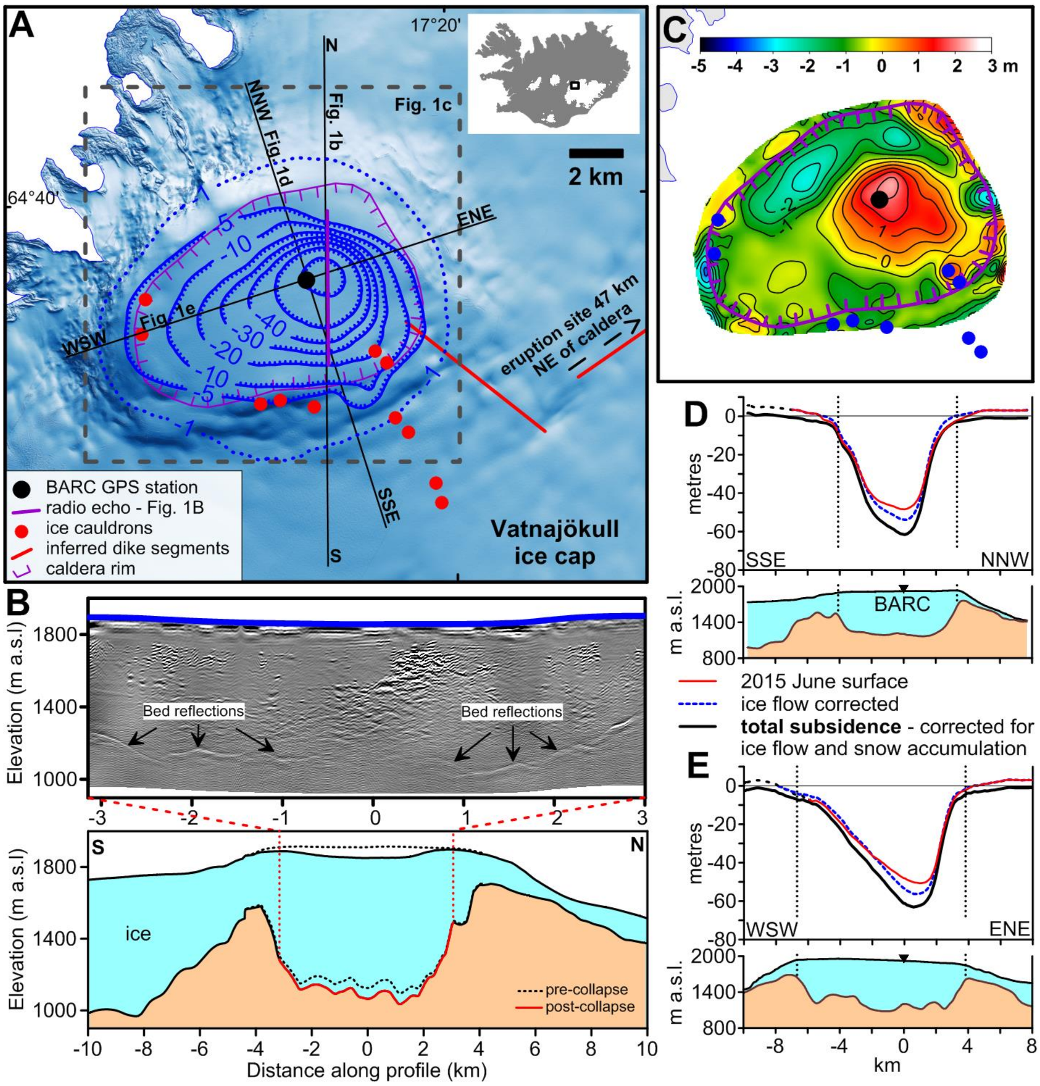

Figure 1. Bárdarbunga and geometry of collapse. A) Map showing the total caldera subsidence (in meters) at the end of collapse in February 2015. The blue dotted line is the 1-m subsidence contour. Minor sustained geothermal activity, monitored from aircraft, increased during the collapse with pre-existing ice cauldrons deepening by up to 50 m and new ones forming at the southern margin and to the southeast of the caldera (*24*). (B) Radio-echo sounding profile from 3 February, 2015, and a cross-section of the caldera showing the collapse. The precollapse topography is obtained by subtracting the subsidence observed at the surface. (C) Modelled changes in ice thickness at the end of February 2015 resulting from ice flow in response to caldera collapse (*24*). D) North-northwest-south-southeast and E) west-southwest-east-northeast cross-sections as measured in June 2015, corrected for winter snow accumulation in 2014-15, measured in June 2015, and modeled vertical ice flow. Subsidence extends 2-3 km beyond the preexisting caldera rims vertical (dotted lines), at shich it amounts to 3-11 m.

The Onset of Collapse

After the initial seismic activity in the caldera receded late on 16 August, seismicity was relatively minor there until 20 August. At the same time our GPS time-series from stations close to the caldera, suggest that deflation of the magma reservoir started on 16 August (*20*). On 20 August, caldera seismicity increased progressively with a series of earthquakes of magnitude M4-M5.8 occurring in the following days (Fig. 2). The first two events occurred on the southern caldera rim (M4.7 on 20 August and M5.1 on 21 August). Following these earthquakes, three similar magnitude events occurred on the northern rim on 23 August, followed by four events on the southern rim on 24-25 August. On 26 August activity shifted again to the northern rim with a M5.8 earthquake, the largest in the whole series. These data indicate that substantial movement on ring faults started on the south side with the 20-21 August earthquakes, then began on the north side on 23 August, and by 24 August the ring faults on both sides where slipping, a process that did not terminate until at the end of February. Onset of collapse therefore likely occurred on 20 August with the ring fault fully activated on 24 August. If we compare the evolution of the dike together with the seismic moment release of the caldera collapse earthquakes, we can clearly see that the dike migration leads the moment release curve (Fig. 2A). We therefore conclude that onset of collapse resulted from a pressure drop in the reservoir as magma was laterally withdrawn into the propagating dike, with the latter possibly primarily driven by regional tectonic tensional stresses (*20*).

The volume of the expanding dike on 20 August had reached approximately 0.25 km^3, increasing to 0.35 km^3 on 24 August (*20*) with the source of this magma being the reservoir beneath the caldera. The relatively minor caldera seismicity on 17-19 August indicates the material overlying the magma reservoir deformed mostly elastically until it reached a critical failure point on 20-24 August. If we assume that the entire volume of eruptible magma within the reservoir was 1.9±0.3 km^3, then the critical volume fraction required to reach the failure point and trigger the collapse (*23*) was 0.12-0.21.

As we recorded the caldera subsidence mainly on the ice (Fig. 1, Fig. S1), we made corrections and additional measurements to derive the underlying bedrock displacement. Our main data on ice surface changes and ice movements are repeated C-band radar altimeter surveys from aircraft, maps made from optical satellite images and the continuously recording GPS station BARC (Bárdarbunga Caldera) that we set up in the center of the caldera on 13 September 2014. The observed velocities and displacements of the ice surface are displayed on Figs. 3A and 3B. We use these observations to constrain three-dimensional Full-Stokes finite element modelling of ice-flow in response to the collapse (*24*). The results show concentric flow, towards the point of maximum collapse within the caldera, with maximum ice thickening at the center of ~3 m by February 2015 (Fig. 1C, Fig. S2). The maximum ice surface lowering of 62±2 m, determined by aerial altimeter surveys, gives a maximum bedrock subsidence of 65±3 m. Our data and models show that apart from the concentric flow towards the deepest part of the subsidence (about 1 km east of BARC) horizontal flow was not much affected (Fig. 3A). We therefore conclude that suggestions of a large increase in ice flow out of the caldera during these events (*25*) cannot be fitted with our data.

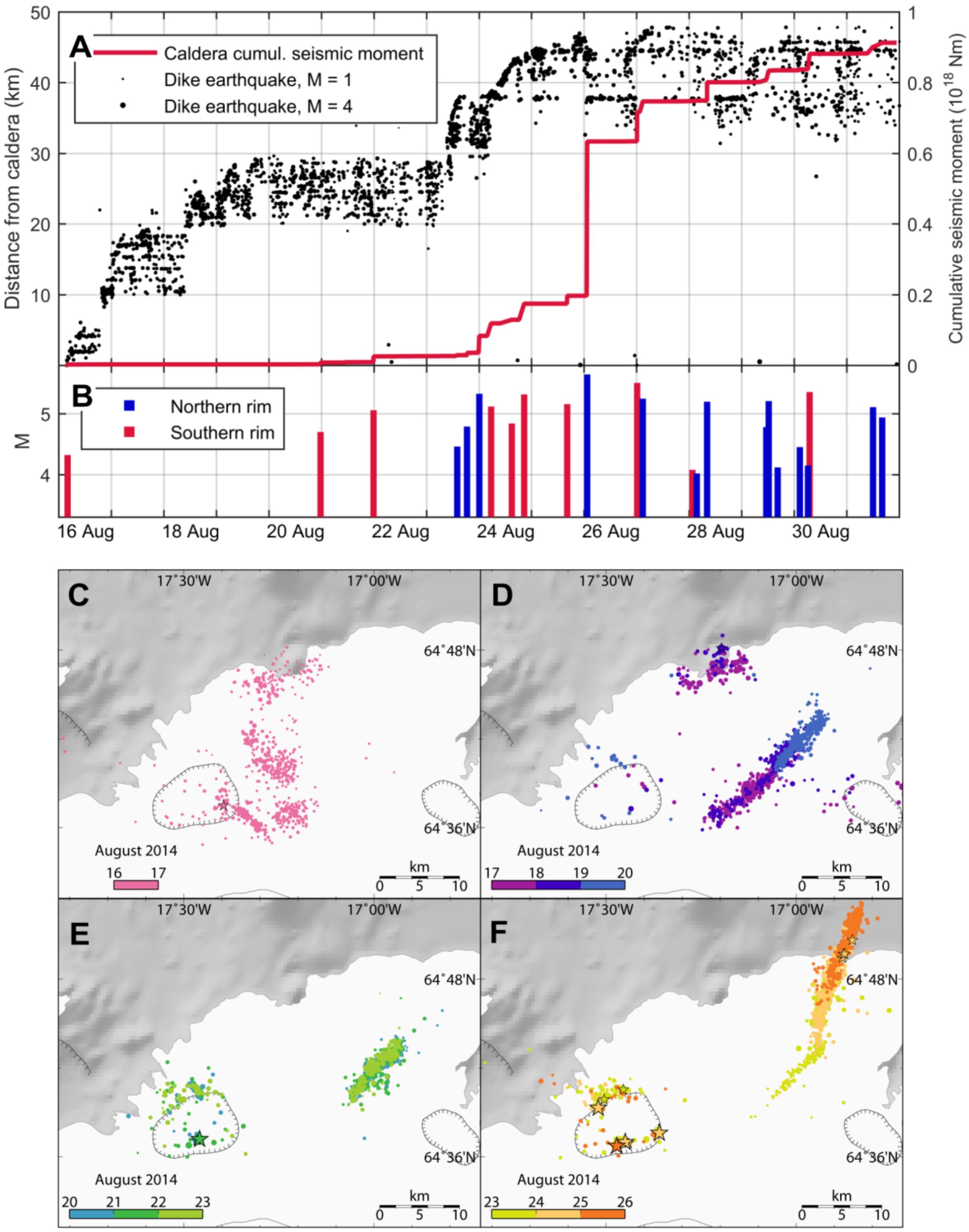

Figure 2. Onset of caldera collapse. A) Cumulative seismic moment release from caldera earthquakes plotted together with distribution of seismicity along the dike length, using high quality relative locations of earthquakes (*20*), for the time period when the dike progressed away from the caldera. Black dots show individual earthquakes, with dot size scaling with magnitude. B) Significant caldera earthquakes with magnitudes above M4 plotted as impulses, where the height represents magnitude and color represents location on southern or northern rim. C) Map of NW Vatnajökull showing earthquake epicenters on 16 August, D) 17-19 August, E) 20-22 August and F) 23-15 August. The stars indicate the larger than magnitude M4 earthquakes in the caldera.

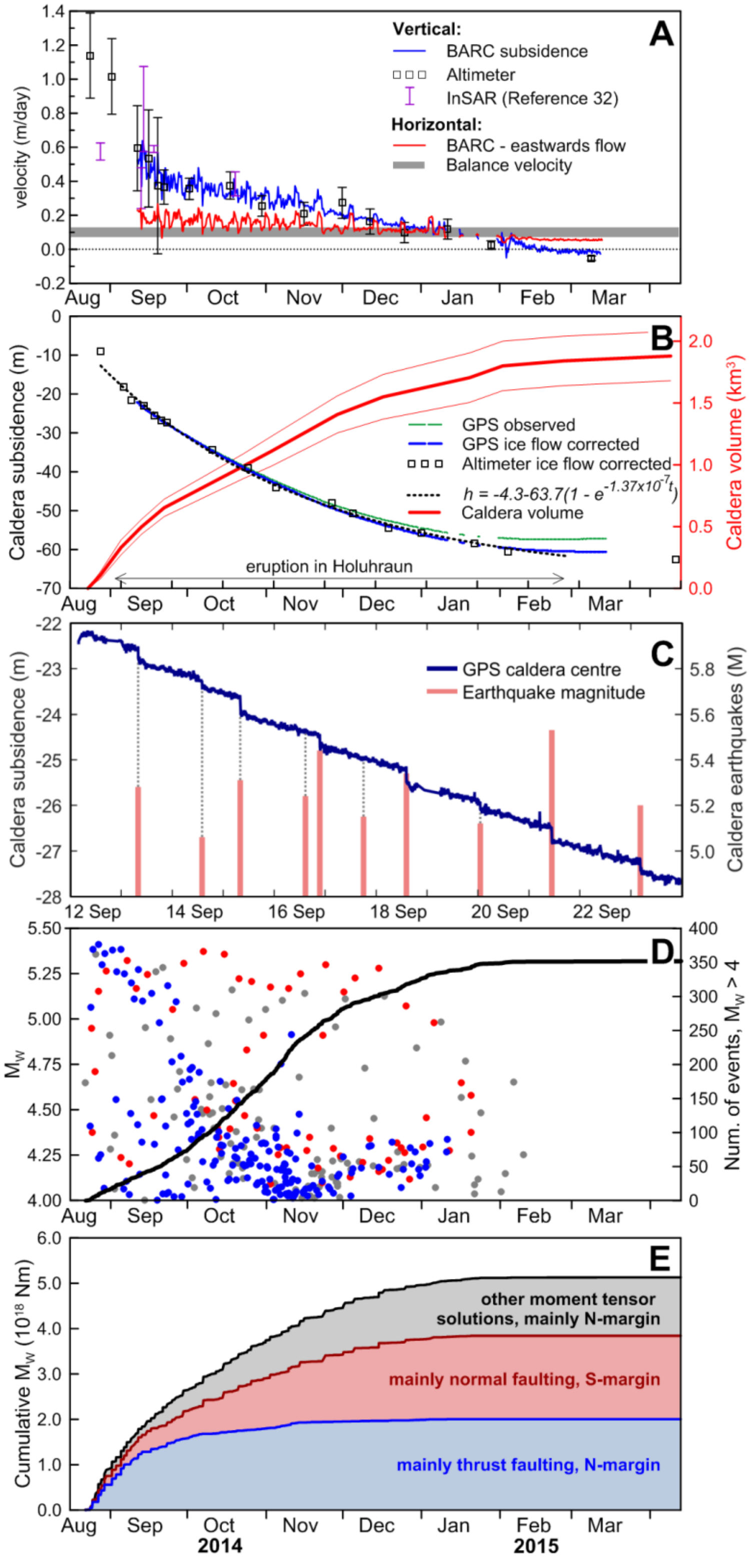

Figure 3. Time series of collapse. A) Vertical and horizontal velocities measured at the BARC GPS station in the center of the caldera (Fig. 1A), including the rate of vertical rate of ice surface subsidence found from altimeter aircraft data and optical satellite photogrammetry. The horizontal balance velocity is obtained by estimating the rate of the eastward ice flow required to transport the net snow accumulation of the glacier to the west of BARC. InSAR-derived vertical velocities are based on (32). B) Subsidence at the center of the caldera and subsidence volume evolution. The volume of the subsidence is obtained by subtracting the mapped surface from the precollapse surface. The caldera subsidence curve is fitted with an equation of the same form as eq. (1). C) High

resolution GPS for 12-23 September, showing M>5 earthquakes coinciding with 20-40 cm rapid collapse, superimposed on gradual subsidence. Note that the size of the steps is influenced by the location of BARC relative to the earthquake centroids, and cannot be used directly to infer the proportion of ring fault slip that ruptured seismically or aseismically. D) Cumulative number of M>4 caldera earthquakes, with magnitude evolution colored in red, blue and grey representing clusters on the southern rim, the northern rim and smaller clusters, respectively (see Fig. S5). E) Cumulative seismic moment for M>4 caldera earthquakes.

Ice Flow, Subsidence Magnitude and Volume

Bedrock subsidence exceeding 1 m occurred within an area of 110 km^2 that extended beyond the pre-existing caldera (Fig. 1, Fig. S1). After termination of collapse the total subsidence at the pre-existing caldera rims amounted to 3 to 11 meters (Fig. 1D and 1E). Using subglacial radio-echo soundings we observed a down-sagged bedrock surface without any clear signs of fault offset (Fig 1B) or indications of water bodies at the ice bedrock interface. The limited resolution resulting from the 600-800 m ice thickness means that we cannot on the basis of the radio-echo results exclude the possibility of steep fault escarpments. However, substantial vertical fault movement at the base of the glacier would result in high strain rates within the basal ice which would instantly fracture the ice fabric and propagate upward. During drainage of subglacial lakes in Iceland, large surface fractures induced by basal motion have been observed repeatedly (*26*) and can serve here as an analog for the possible surface manifestations of vertical basal motion. The absence of such surface ice fractures at Bárdabunga indicates that no substantial fault escarpment formed at the bottom. The calculated collapse volume is 1.8±0.2 km^3, not significantly different from the combined volume of erupted and intruded magma (Fig. 3B).

Magma reservoir depth

Lava chemistry, surface gas composition and geodetic modelling indicate drainage of a magma reservoir at a depth of ~12 km. The erupted lava is typical olivine tholeiite with a relatively uniform chemical composition, consistent with efficient homogenization of melts before eruption. Several independent geobarometers (Fig. 4) yield an equilibrium pressure of 350-550 MPa, indicating that melt resided at depths of 11-16 km before the eruption. We obtained a similar result (14±3 km) from analysis of subaerial gas measurements (Fig. 4). This depth concurs with our regional geodetic observations, which are dominated by a deflating source at 8-12 km depth beneath Bárdarbunga, after the cessation of dike-related deformation in mid-September (Figs. S3 and S4).

Seismicity and subsurface structure

We used seismic data and Distinct Element Method (DEM) numerical modelling (*24*), to characterize the deeper collapse structure as the reactivation of a steeply-inclined ring fault (Fig. 5). We mostly observed seismicity at depths of 0-9 km beneath the northern and southern caldera rims (Fig. 5B), with earthquakes being more numerous on the northern rim. This spatial pattern of seismicity is consistent with fracturing above a deflating magma reservoir that was elliptical in plan-view (*27*). In cross-section, the hypocenters indicate a steeply (~80°) outwards-dipping fault in the northern cluster, while the southern cluster they indicate a vertical or near-vertical fault dip. A series of DEM forward simulations of a magma reservoir and ring fault system, as constrained by the hypocenter distribution and by the geobarometry data, tested the above structural interpretation against the observed NNW-SSE subsidence profile. The models indicate that a pre-existing and relatively low friction (coefficient of 0.1-0.2) ring-fault system controlled the subsidence at depth (Fig. 5C, D). Our best fitting models had preexisting faults dipping out at 80-85° away from the caldera center on the north side and at 85-90° toward the caldera center on the south side. The modeled pre-existing faults lay at 1-2 km below the surface on the north side and 3-4 km on the south side. Modeling of a more complex fault geometry or the inclusion of greater material heterogeneity may further improve the data fit, but presently lacks robust geophysical constraints. The arrangement of an outward dipping fault on one side of a caldera and an inward-dipping fault on the other is typical of ‘asymmetric’ or ‘trapdoor-like’ collapses produced in past analog and numerical modeling studies (*8*, *28*, *29*). It also occurs at Glencoe (*29*) and Tendurek (*30*) volcanoes . Finally, our finding is consistent with past seismological results that defined a very similar ring-fault geometry during the last period of activity at Bardarbunga in 1996 (*31*).

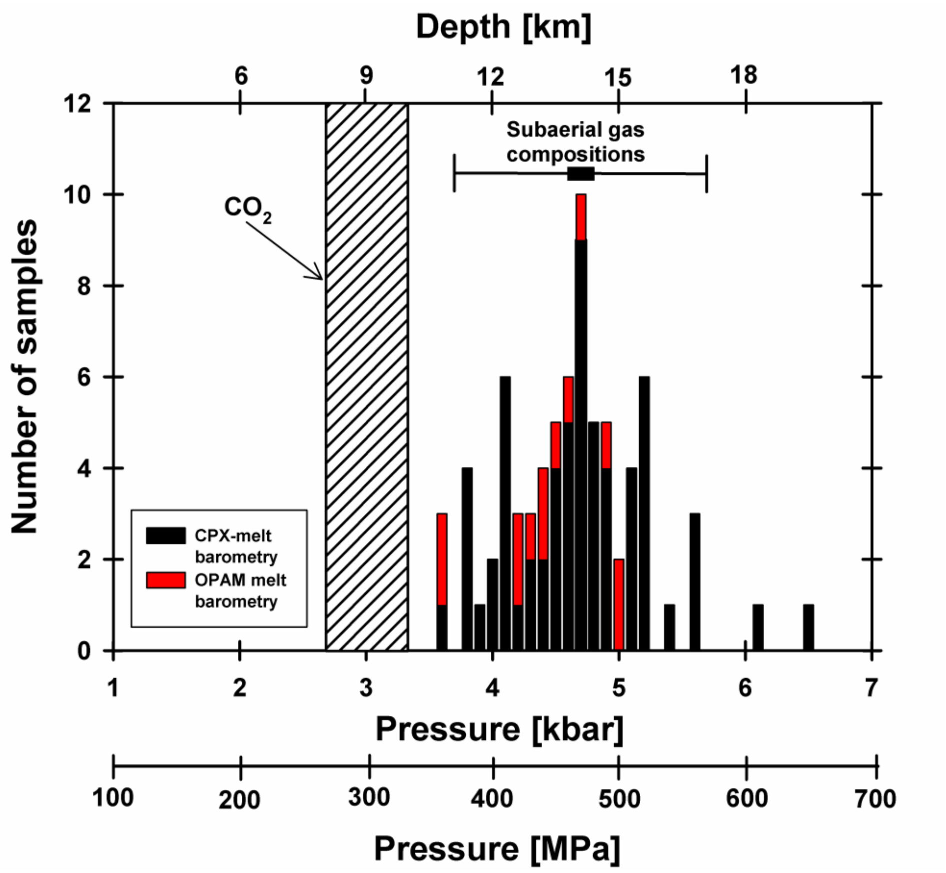

Figure 4. Magma reservoir depth from geobarometric and subaerial gas analysis. The vertical shaded-bar crossing the graph, indicates the minimum pressure obtained (~300MPa) from density barometry of plagioclase hosted CO2-bearing fluid inclusions. Due to postentrapment modifications of fluid inclusions during magma ascent, this value is likely an under-estimate, as indicated by the dashed arrows. The results from the analysis of subaerial gas compositions are based on FTIR and MultiGAS measurements (24).

Through regional moment tensor (MT) inversion, we infer that the source mechanisms of 77 M>5 events (Fig. S5) confined to two clusters beneath the northern and southern rim regions show contributions of both shear and non-shear components. The shear components indicate possible ruptures of segments on the ring fault. Shear failure on inward dipping ring faults, or the sudden injection of magma in horizontal fissures forming sills have been proposed (*32*) to explain the shear components of the observed earthquakes at Bárdarbunga. We, however, narrowed down on plausible solutions by using the micro-earthquakes (Fig. 5A). The moment tensor solutions are well constrained, but the inferred dip of the shear plane we obtain is uncertain since the non-shear component, in this case a negative, sub-vertical compensated linear vector dipole (vCLVD), is dominant. As a result, the shear orientation obtained depends very much on the decomposition approach.

By using the constraint of the steeply outward dipping ring fault on the northern cluster we derive a MT solution that is a combination of a negative vCLVD and steep E-W striking reverse faulting (Fig. 3D, 3E and Fig. S5). In contrast, standard decomposition of the northern cluster MTs provides normal faulting along steep N-S striking planes, a result that is inconsistent with the observed main fault orientation. The southern cluster MTs are consistent with being composed of families (*33*) of steep normal faulting earthquakes.

The large, negative vCLVD indicates a combination of downward contraction and horizontal expansion, as has been observed in mines as well as in volcanic calderas during collapses (e.g. *31*, *34*). This could imply failure of support structures directly above or even within the magmatic reservoir, or the sudden response of the reservoir fluid to vertical compression.

Temporal development of subsidence and related seismicity

Subsidence occurred gradually during the eruption (Fig. 3B). From an initial rate in the caldera center of ~1 m/day during the first 20 days (Fig. 3B), subsidence declined in a near exponential manner with time (24). Subsidence terminated when the eruption ended in February 2015. We can associate some of the M>5 caldera earthquakes, during the first couple of months of activity, with drops of 10-40 cm, but subsidence was otherwise continuous (Fig. 3C). The gradual decline in the rates of subsidence and caldera volume growth is mirrored by a decline in the cumulative seismic moment, the latter reflecting a decrease in the number of larger earthquakes with time (Fig. 3D, 3E). Nonetheless, in terms of the cumulative seismic moment of 5.07×10^{18} Nm for the M>4.0 events, this collapse is the second largest recorded, after that of Katmai (1912) (*35*). The geodetic moment depends on the shear modulus, the fault area and the amount of slip assumed. The shear modulus could be very low in regions of intense faulting such as on a caldera ring fault. The possible range of the geodetic moment is found by considering a ring fault reaching from the surface to 12 km depth, 60 m of slip and a shear modulus over a wide range, 2-20 GPa. This results in a moment of 4×10^{19} - 4×10^{20} Nm, or 10-100 times the cumulative seismic moment of the earthquakes. This difference is consistent with the modeling of surface deformation observed during one of the events (Fig S7).

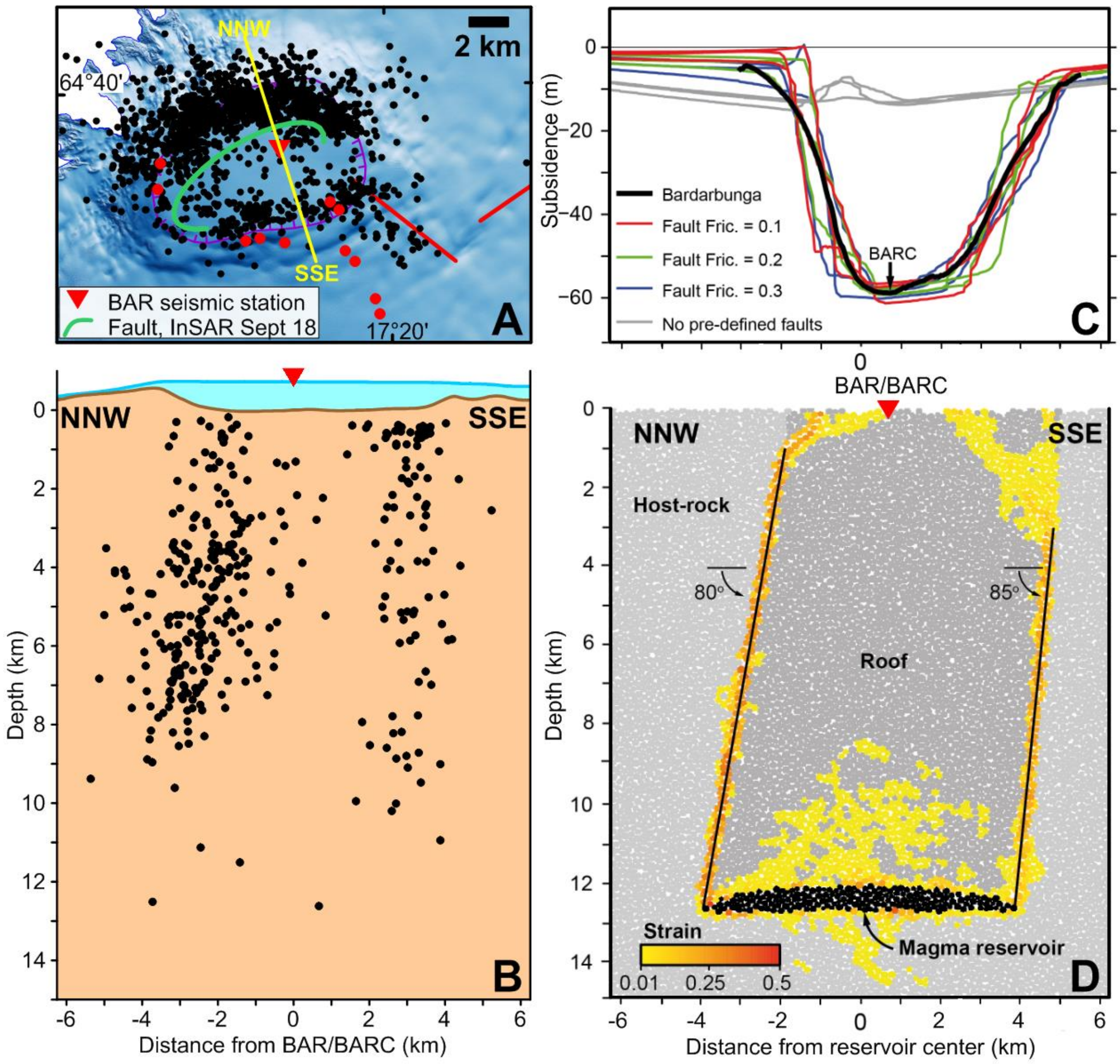

Figure 5: Fault geometry and collapse modelling: A) Earthquakes 1 August – 17 October 2014, B) seismicity along a 2-4 km wide strip on the NNW-SSE cross section, depth relative to bedrock caldera floor. C-D) Two-dimensional DEM modeling of the collapse, constrained by subsidence geometry, earthquake locations in (B), and the geobarometry (Fig. 4). The geometry illustrated in (D) obtained the best agreement with the observations. The color scale shows the maximum finite shear strain. Surface displacement profiles for different preexisting fault frictions are provided in (C). Three model realizations are shown for each friction value.

Caldera-flowpath interaction and piston collapse modeling

We see a short-term (multihourly) mechanical coupling of the collapsing caldera and the distal dike (south of eruption site) in the timing of earthquakes in the dike and at the caldera (Fig. 6A). Within a six-hour window before and after large caldera earthquakes the frequency of dike earthquakes was increased relative to background rate (24). We observed this pattern in the data after the beginning of October 2014, when the dyke had stopped propagating and a quasi-steady magma flow path had developed, until February 2015 when seismic activity stopped. For the three hours after caldera earthquakes with magnitude M > 4.6, as well as for the three hours before caldera earthquakes with M > 4.0, the increase in seismicity was significant (*24*) (p = 0.05; Fig. 6, Fig. S8).

At Bárdarbunga communication therefore existed between caldera subsidence events and pressure changes in a conduit up to 48 km away. Spatiotemporal patterns of tilt at Kilauea Volcano, Hawaii, show a similar phenomenon that can be explained by the propagation of pressure transients within an elastically deformable dyke (*36*). By analogy, we can make the interpretation that caldera earthquakes may generate a pressure pulse that leads to increased seismicity at the end of the dike. The communication could be two-way, although it is difficult to explain a pressure pulse from the dike towards the caldera. One possibility is that readjustment of the dike (e.g. sudden unblocking) can increase the dike volume slightly and subsequently lower the magma pressure which then translates back to the caldera. The communication may also be entirely one-way, from the caldera to the dike: smaller caldera earthquakes, and/or aseismic deformation at depth just above the magma reservoir may precede a large caldera earthquake, increasing dike pressure and dike seismicity.

We explain the longer term (weeks to months scale) coupling in the form of the gradually declining rates of caldera subsidence, caldera volume change and lava eruption (Figs. 3B, 6B) with a model of a collapsing piston overlying a pressurized magma reservoir. We assume that the reservoir pressure and fault friction each partially support the piston weight (*24*). Drainage of magma reduces the reservoir pressure and causes piston subsidence (Fig. S6). This in turn raises the reservoir pressure, leading to a feedback loop that maintains quasi-constant pressure at the magma reservoir top, and drives further magma drainage. The pressure feeding the eruption drops, however, due to the reduction in hydraulic head of magma over time. Kumagai et al. (37) also used a piston model to explain caldera collapse at Miyakejima in 2000, but in their model no change in hydraulic head was assumed and outflow rate was held constant.

Assuming that the time-averaged resistive force due to friction on the ring faults remains constant, and that magma flow is laminar through a cylindrical pipe with radius *r*, and conduit length *L*, with L>>r, then

$$\Delta P \approx \Delta P_0 e^{-\frac{\pi \rho g r^4}{8A\eta L}t} \qquad (1)$$

Where ΔP is the driving overpressure, ΔP_0 is the initial driving overpressure, ρ is the density of the magma, g is gravitational acceleration, A is the cross-sectional area of the magma reservoir, η is the dynamic viscosity of the magma and t is time (*24*). We estimated ΔP_0 and the constant in the exponent, assuming that the measured subsidence within the caldera represents the decrease in magma reservoir height with time (Fig 3B). Note, this represents a minimum estimate for ΔP_0, as there may also have been dilation at depth. The model also fits the measured caldera volume change (Fig. 3B) and eruption rate (Fig. 6B). This model predicts the same form of decay in flow rate (exponential) as the standard 'Wadge' model of depressurisation of an overpressured magma body (*38*), but by a different mechanism. The feedback mechanism of re-pressurisation from the ongoing piston collapse enhanced the length and speed of dike propagation, and the duration of the eruption. In this model, therefore, both the eruption drives the collapse and collapse drives the eruption.

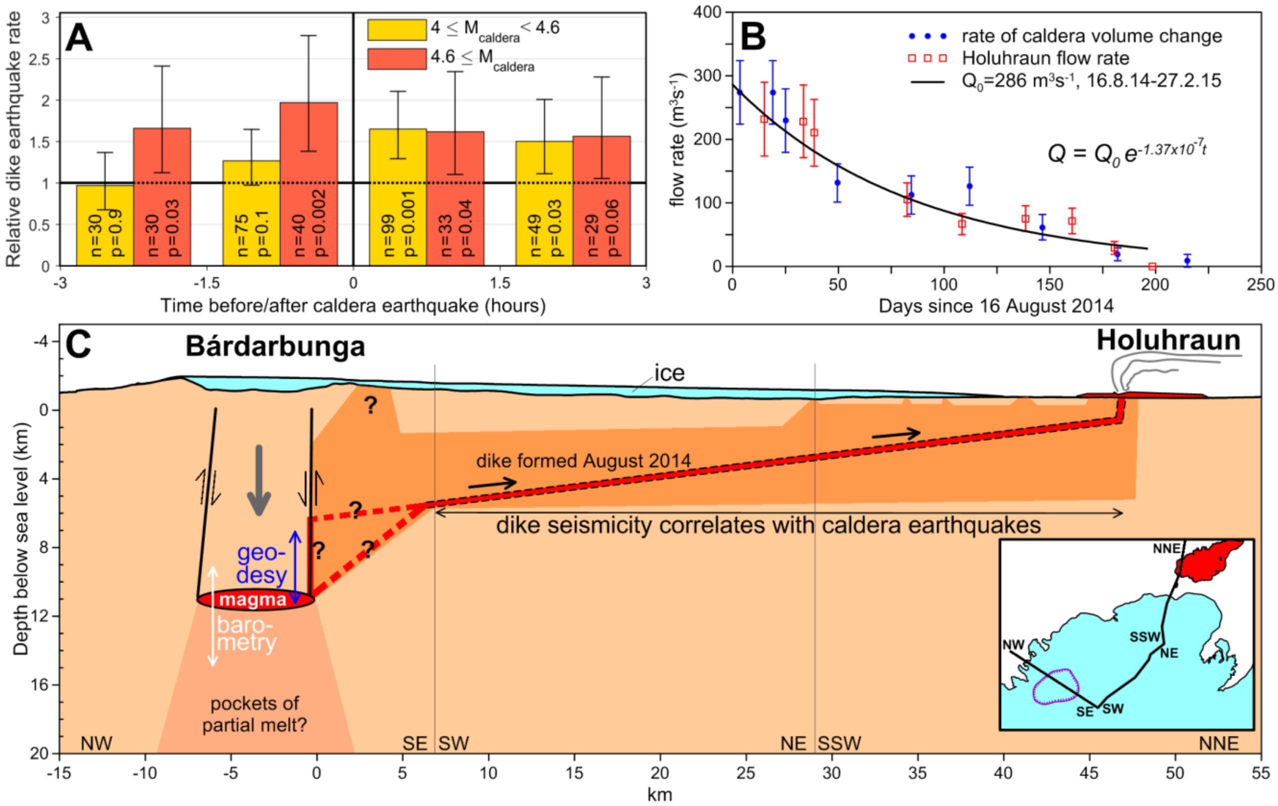

Figure 6. Caldera - magma flowpath interaction. A) Rate of dike earthquakes relative to background levels before and after significant caldera earthquakes of magnitude >M4. The p-values indicate the two sided significance and n is the number of earthquakes used. Error bars indicate 90% confidence intervals (24). B) Exponential model of magma flow rate constrained by caldera GPS subsidence (*24*) compared with rate of volume change in caldera and eruption rate in Holuhraun. The eruption stopped on Day 194 (27 February, 2015) before the driving pressure reaches zero, as expected if the conduit becomes clogged by solidifying magma as the flow rate drops. Caldera subsidence also terminated around the end of February (see GPS ice-flow corrected subsidence in Fig. 3B). C) Schematic cross-section of caldera - magma reservoir - pipe-like magma flow path and eruption site after dike formation (*20*, *21*). The inferred magma reservoir is set at 12 km below bedrock caldera floor. It is possible that magma ascended first along the ring fault before forming the dyke above 6-10 km depth. We indicate the constraints on depth to magma chamber from geobarometry with a white arrow and from geodesy with a blue arrow.

Overview and implications

Table 1 contextualizes the key features of the 2014-15 Bardarbunga collapse with respect to those of the six other collapses instrumentally monitored to date. The areal extent of the Bardarbunga collapse (110 km^2) is the largest yet observed historically and is comparable to that associated with major silicic eruptions in the geological record (6). The total subsidence (65 m) is one to two orders of magnitude smaller than all past collapses listed here, but the large area means that it has the fourth largest collapse volume (1.8 km^3) overall. The erupted volume (1.4 km^3) is the largest of the observed mafic collapses so far, although considerable uncertainty surrounds the volumes associated with the collapse of Fernandina. In volume terms, both the silicic eruptions and collapses of Katmai and Pinatubo were twice to six times larger. The cumulative seismic energy release at Bardarbunga (25×10^{13} J, see Table 1) is dwarfed by that of Katmai (1600×10^{13} J) but is similar to Miyakejima (22×10^{13} J), despite the much smaller area of the latter (1.9 km^2). This is explained by the much greater subsidence at Katmai (>1200 m). The gradual collapse of Bardarbunga had the second longest duration (190 days) yet recorded. Only the duration of collapse at Tolbachik (515 days) exceeds it. Finally, Bardarbunga has the longest confirmed length of an associated lateral intrusion (48 km) and the longest distance to the main vent (40 km).

Table 1: Instrumentally-monitored caldera collapses since 1900 AD.

References for data: ***Bardarbunga:*** (*20*); this study; ***La Reunion:*** (*12,16,44-46*); ***Miyakejima:*** (*2, 11, 34, 47-49*); ***Tolbachik:*** (*50-53*); ***Fernandina:*** (*2, 9, 54*); ***Katmai:*** (*35, 41, 55*); ***Pinatubo:*** (*2, 15, 42, 43, 56*)

Volcano	Year	Magma	Maximum subsidence (m)	Collapse duration (days)	Collapse area (km^2)	Collapse volume (km^3)	Reservoir depth (km)	Intrusion volume (km^3)†	Erupted volume (km^3)‡	Total magma volume (km^3)	Distance to vent (km)§	Intrusion length (km)‖	Seismic energy ($\times 10^{13}$ J)¶	Max. EQ#
Bárdarbunga	2015	Basalt	~65	190	110	1.8	11–16	0.5	1.4	1.9	40	48	25	5.8
La Reunion	2007	Basalt	~450	2	0.82	0.1	2–3	0.02	0.14	0.16	7	7	?	3.2
Miyakejima	2000	Basalt	~1600	40	1.9	0.6	4–7	1.2	0.01	1.21	5.6	35	22	5.6
Tolbachik	1976	Basalt	>500	515	2.5	0.35	4–6?	?	1.2	>1.2	28	~45	?	2.9
Fernandina	1969	Basalt	~350	12	7	2	?	?	0.2	>0.2	10.5?	10.5?	2	5.2
Katmai	1912	Rhyolite	>1300	3	8.8	5.5	2–5	?	*13.5*	*>13.5*	10	10	*1600*	*7*
Pinatubo*	1991	Dacite	*~900*	*2*	*4*	*2*	*7–11*	*?*	*4.5*	*4.5*	*1*	*4*	*2*	*5.7*

*All caldera collapses except Pinatubo formed in association with lateral withdrawal and intrusion of magma. †Intrusion volume values are typically constrained by inversions of data from geodetic networks and so are available only for the most recent events. ‡Erupted volumes are given as dense-rock equivalent—i.e., with porosity removed. §Distance measured from center of caldera to the most distant known vent active during collapse. ‖Estimated horizontal length of the intrusion, from locations of seismicity and/or inversions of geodetic data in all cases except Katmai. For Katmai and Fernandina, intrusion length is estimated as the distance from caldera to vent and is hence a minimum value. ¶Cumulative seismic energy release calculated by converting the cumulative scalar moments (M_0) by using a factor of 5×10^{-5} [from an energy-moment relationship determined by Kanamori *et al*. (*57*)]. #Maximum earthquake magnitude (EQ) associated with caldera formation. Magnitude determined from surface waves (M_s) is given for Tolbachik (*53*), Katmai (*35*), and Fernandina (*54*). For La Reunion, Earthquake duration magnitude (M_d) is used (*12*, *44*). For Miyakejima and Bárdarbunga, the maximum moment magnitude (M_w) for collapse-related very-long-period events is given (*34*, *58*, this study).

Our data and modelling show that withdrawal and eruption of magma triggered the collapse at Bardarbunga. For the likely depth to diameter ratio of the magma reservoir, the critical volume fraction required to trigger the onset of collapse (0.12-0.21) was much lower than that predicted by past analytical and analogue modelling (*23*, *39*). A similar inference of low critical volume fractions at La Reunion and Miyakejima (*16*) was explained as a consequence of the reactivation of pre-existing ring faults, a proposition in line with our observations and analysis of the Bardarbunga collapse.

Nonetheless, we also show that there is a tight mechanical interplay between collapse and eruption throughout the process once collapse has started, with eruption driving collapse and vice versa on both hourly and eruption-long time scales. For the longer time-scale coupling, the results also show that the physical properties of both the magma reservoir roof and the magma pathway regulate caldera collapse and magma outflow rate. Consequently, collapse at Bárdarbunga occurred gradually and at a steadily (exponentally) declining rate. This is a very similar pattern to that inferred for the 1968 Fernandina collapse (*2*, *16*). In contrast to some model predictions (*40*) and to the 2007 collapse of Piton de la Fournaise (*16*), we found no evidence for rapid and sustained pressure increase in the magma reservoir as a result of collapse, possibly due to substantial ductile behavior of the roof of the larger and deeper Bardarbunga magma reservoir (*13*, *16*).

The question of whether or to what extent our understanding of caldera collapse at mafic volcanoes such as Bardarbunga is transferrable to large silicic systems remains an open one. On the one hand the gradual nature of collapse at Bardarbunga and Fernandina contrasts with the highly punctuated collapse style inferred during explosive silicic eruptions like Katmai and Pinatubo (*2*, *41*). In addition, collapse at silicic volcanoes is generally considered to be triggered by eruption through a central vent rather than through the lateral withdrawal mechanism seen at Bardarbunga. On the other hand, the most silicic of all instrumentally monitored collapses, Katmai, was also clearly associated with a lateral withdrawal. This mechanism could therefore be more widespread at silicic calderas than commonly considered. Furthermore, the punctuated collapse style inferred for the Katmai and Pinatubo cases rests on large (M5-7) earthquakes that yield dramatic steps in a curve of cumulative seismic release against time (2).The locations and source mechanisms of these apparently collapse-related earthquakes are poorly constrained, however. As best highlighted in the case of Pinatubo, a regional tectonic origin for them cannot be precluded (*15*, *35*, *42*, *43*). Consequently, Bardarbunga 2014-15 provides our clearest picture yet of how caldera collapse can be triggered during large eruptions, and how the dynamics of the subterranean magma flow path and the interaction with magma reservoir pressure regulates eruption rates and the rate of collapse.

Materials and methods

We mapped changes in ice surface topography with time by using aircraft-based radar altimetry, satellite optical photogrammetry, and a continuously recording GPS station installed on the ice surface. We modeled the ice flow within the caldera by using a full-Stokes finite element model constrained by the horizontal GPS velocities. We measured the caldera bedrock topography through radio-echo sounding. We mapped changes in lava volume with a ground-based theodolite and aircraft altimetry. Bulk density of the lava was determined from gravity profiles. We used interferometric synthetic aperture radar (InSAR) to determine coseismic ground deformation at the caldera for several 24-hour periods spanning large caldera earthquakes. We ran elastic dislocation models of this deformation to infer the location of faults that slipped during the earthquakes.Microearthquakes (M. 2) at the caldera were recorded by the Icelandic national seismic network and relatively relocated by using a standard 1D velocity model. The microearthquakes were shifted southward by using the faults inferred from the InSAR modeling. We performed a regional moment tensor inversion for all events with M > 5, adopting a full (MT point source approximation and elucidating double-couple, compensated linear vector dipole and isotropic components. We extended the interpretation of source processes to smaller events by applying a waveform similarity analysis, and we more precisely determined locations by using relative location techniques. We evaluated the role of preexisting ring-fault structures on collapse by using 2D DEM modeling. We determined the approximate depth of the magma reservoir from a point-pressure source model in an elastic half space, constrained by post-rifting InSAR and GPS data. We computed caldera-dike seismicity correlations by calculating the number of dike earthquakes in 1.5-hour bins before and after large caldera earthquakes; P values were computed with a likelihood ratio test. We analyzed major element compositions of minerals and glasses by using an electron microprobe. Fluid inclusions within phenocrysts were analyzed by optical microscopy and confocal Raman spectroscopy. Three independent thermobarometers constrained the depth of magma accumulation before the onset of the eruption: glass thermobarometry, clinopyroxene-liquid thermobarometry, and CO2 density barometry. We also measured the composition of subaerial eruptive gases on multiple occasions with an open-path Fourier transform infrared spectrometer (FTIR) and a multicomponent gas analyzer system (Multi-GAS). Finally, we modeled caldera subsidence and eruption rate by considering analytically a collapsing piston overlying a pressurized magma reservoir and driving magma flow through a cylindrical pipe.

References

1. M. Branney, V. Acocella, "Calderas" in *The Encyclopedia of Volcanoes*, H. Sigurdsson, B. Houghton, H. Rymer, Eds. (Academic Press, Academic Press, Heidelberg, Amsterdam, Boston, ed. 2, 2015), pp. 229-315.

2. J. Stix, T. Kobayashi, Magma dynamics and collapse mechanisms during four historic caldera-forming events. *J. Geophys. Res.* **113**, JB005073 (2008).

3. A. R. McBirney, A historical note on the origin of calderas. *J. Volcanol. Geotherm. Res.* **42**, 303-306 (1990).

4. R. S. J. Sparks, P.W. Francis, R. D. Hamer, R. J. Pankhurst, L. O. O'callaghan, R. S. Thorpe, R. Page, Ignimbrites of the Cerro Galán caldera, NW Argentina. *J. Volcanol. Geotherm. Res.* **24**, 205-248 (1985).

5. T. H. Druitt, R. S. J. Sparks, On the formation of calderas during ignimbrite eruptions. *Nature* **310**, 679-681 (1984).

6. P. W. Lipman, Subsidence of ash-flow calderas: relation to caldera size and magma-chamber geometry. *Bull. Volc*., **59**, 198-218 (1997).

7. V. Acocella, Understanding caldera structure and develpoment: an overview of analogue models compared to natural calderas. *Earth Sci. Rev*., **125**, 125-160 (2007).

8. O. Roche, T. H. Druitt, O. Merle, Experimental study of caldera formation. *J. Geophys. Res.* **105**, 395-416 (2001).

9. T. Simkin, K. A. Howard, Caldera collapse in the Galapagos Islands, 1968: The largest known collapse since 1912 followed a flank eruption and explosive volcanism within the caldera. *Science* **169**, 429–437 (1970).

10. S. A. Fedotov, Y. K. Markhinin, *The Great Tolbachik Fissure Eruption. Geological and Geophysical Data 1975-1976.* (Cambridge University Press, Cambridge, 2011).

11. N. Geshi, T. Shimano, S. Chiba, Caldera collapse during the 2000 eruption of Miyakejima Volcano, Japan. *Bull. Volcanol*. **64**, 55-68 (2002).

12. T. Staudacher, V. Ferrazzini, A. Peltier, P. Kowalski, P. Boissier, P. Catherine, F. Lauret, F. Massin, The April 2007 eruption and the Dolomieu crater collapse, two major events at Piton de la Fournaise (La Réunion Island, Indian Ocean). *J. Volcanol. Geotherm. Res*. **184**, 126-137 (2009).

13. E. P. Holohan, M. P. J. Schöpfer, J. J. Walsh, J. J. Stress evolution during caldera collapse. Earth Planet. Sc. Lett. **421**, 139-151 (2015).

14. K. V. Cashman, G. Giordano, Calderas and magma reservoirs. *J. Volcanol. Geotherm. Res*. **288**, 28-45 (2014).

15. J. Battaglia, C. H. Thurber, J.-L. Got, C. A. Rowe, R A. White, Precise relocation of earthquakes following the 15 June 1991 eruption of Mount Pinatubo (Philippines). *J. Geophys. Res*. **109**, B7 (2004).

16. L. Michon, F. Massin, V. Famin, V. Ferrazzini, G. Roult, Basaltic calderas: Collapse dynamics, edifice deformation, and variations of magma withdrawal. *J. Geophys. Res*. **116**, B3 (2011).

17. H. Björnsson, P. Einarsson, Volcanoes beneath Vatnajökull, Iceland: evidence from radio-echo sounding, earthquakes and jökulhlaups. *Jokull* **40**, 147-148 (1990).

18. M. T. Gudmundsson, T. Högnadóttir, Volcanic systems and calderas in the Vatnajökull region, central Iceland, constraints on crustal structure from gravity data. Journal of Geodynamics, 43, 153-169 (2007).

19. T. Thordarson, G. Larsen, Volcanism in Iceland in historical time: Volcano types, eruption styles and eruption history. *J. Geodyn*. **43**, 118-152 (2007).

20. F. Sigmundsson, A. Hooper, S. Hreinsdóttir, K. S. Vogfjörd, B. G. Ófeigsson, E. R. Heimisson, S. Dumont, M. Parks, K. Spaans, G. B. Gudmundsson, V. Drouin, T. Árnadóttir, K. Jónsdóttir, M. T. Gudmundsson, T. Högnadóttir, H. M. Fridriksdóttir, M. Hensch, P. Einarsson, E. Magnússon, S. Samsonov, B. Brandsdóttir, R. S. White, T. Ágústsdóttir, T. Greenfield, R. G. Green, A. R. Hjartardóttir, R. Pedersen, R. A. Bennett, H. Geirsson, P. C. La Femina, H. Björnsson, F. Pálsson, E. Sturkell, C. J. Bean, M. Möllhoff, A. K. Braiden, E. P. S. Eibl, Segmented lateral dyke growth in a rifting event at Bárðarbunga volcanic system. *Nature* **517**, 191-195 (2015).

21. T. Ágústsdóttir, J. Woods, T. Greenfield, R. G. Green, R. S. White, T. Winder, B. Brandsdóttir, S. Steinthórsson, H. Soosalu, Strike-slip faulting during the 2014 Bárðarbunga-Holuhraun dike intrusion, central Iceland. *Geophys. Res. Lett*. (accepted). DOI: 10.1002/2015GL067423

22. S. R. Gíslason, G. Stefánsdóttir, M. A. Pfeffer, S. Barsotti, Th. Jóhannsson, I. Galeczka, E. Bali, O. Sigmarsson, A. Stefánsson, N. S. Keller, A. Sigurdsson, B. Bergsson, B. Galle, V. C. Jacobo, S. Arellano, A. Aiuppa, E. S. Eiríksdóttir, S. Jakobsson, G. H. Gudfinnsson, S. A. Halldórsson, H. Gunnarsson, B. Haddadi, I. Jónsdóttir, Th. Thordarson, M. Riishuus, Th. Högnadóttir, T. Dürig, G. B. M. Pedersen, A. Höskuldsson, M. T. Gudmundsson, Environmental pressure from the 2014–15 eruption of Bárðarbunga volcano, Iceland. *Geochem. Perspect. Lett*., **1**, 84-93 (2015).

23. O. Roche, O., T. H. Druitt, Onset of caldera collapse during ignimbrite eruptions. Earth Planet. Sci. Lett., **191**(3), 191-202 (2001).

24. Materials and methods are available as supplementary materials on Science Online.

25. J. Browning, A. Gudmundsson, Surface displacements resulting from magma-chamber roof subsidence, with application to the 2014-2015 Bardarbunga-Holuhraun volcanotectonic episode in Iceland. *J. Volcanol. Geotherm. Res*. **308**, 82-98 (2015).

26. H. Björnsson, Hydrology of ice caps in volcanic regions. Soc. Sci. Isl. 45, 139pp (1988).

27. E. P. Holohan, V. R. Troll, B. Van Wyk de Vries, J. J. Walsh, T. R. Walter, Unzipping Long Valley: an explanation for vent migration during an elliptical ring fracture eruption. *Geology* **36**, 323-326 (2008).

28. E. P. Holohan, T. R. Walter, M.P. Schöpfer, J. J. Walsh, B. Wyk de Vries, V. R. Troll, Origins of oblique-slip faulting during caldera subsidence. J. Geophys. Res. **118**(4), 1778-1794 (2013).

29. C. Clough, H. Maufe, E. Baley, The cauldron subsidence of Glen-Coe, and the associated igneous phenomena. Q.J.Soc. Lond. **65**, 611–678 (1909).

30. H. Bathke, M. Nikhoo, E.P. Holohan, T.R. Walter, Insights into the 3D architecture of an active caldera ring-fault at Tendürek volcano through modeling of geodetic data. Earth. Planet. Sci. Lett. **422**:157-168 (2015).

31. A. Fichtner, H. Tkalcic, Insights into the kinematics of a volcanic caldera drop: Probabilistic finite-source inversion of the 1996 Bardarbunga, Iceland, earthquake. *Earth Planet. Sc. Lett*. **297**, 607-615 (2010).

32. B. Riel, P. Milillo, M. Simons, P. Lundgren, H. Kanamori, H., S. Samsonov, The collapse of Bárðarbunga Caldera, Iceland. *Geophys. J. Int*. **202**, 446-453 (2015).

33. S. Cesca, A. T. Sen, T. Dahm, Seismicity monitoring by cluster analysis of moment tensors. *Geophys. J. Int*. **196**, 1813-1826 (2013).

34. A. Shuler, G. Ekström, M. Nettles, Physical mechanisms for vertical-CLVD earthquakes at active volcanoes. J. Geophys. Res. **118**(4), 1569-1586 (2013).

35. K. Abe, Seismicity of the caldera-making eruption of Mount Katmai, Alaska in 1912. *B. Seismol. Soc. Am*. **82**, 175-191 (1992).

36. C. P. Montagna, H. M. Gonnermann, Magma flow between summit and Pu`u `O`o at Kilauea Volcano, Hawaii. *Geochem. Geophy. Geosy.* **14**, 2232–2246 (2013).

37. H. Kumagai, T. Ohminato, M. Nakano, M. Ooi, A. Kubo, H. Inoue, J. Oikawa, Very-long-period seismic signals and caldera formation at Miyake Island, Japan. Sci. 293, 687-690 (2001).

38. G. Wadge, Steady state volcanism: evidence from eruption histories of polygenetic volcanoes. J. Geophys. Res. **87**, B5: 4035-4049 (1982).

39. A. Geyer, A. Folch, J. Martí, Relationship between caldera collapse and magma chamber withdrawal: an experimental approach. J Volcanol. Geotherm. Res. **157**, 375-386 (2006).

40. A. Folch, J. Marti, Time-dependent chamber and vent conditions during explosive caldera-forming eruptions. *Earth Planet. Sc. Lett.* **280**, 246-253 (2009).

41. W. Hildreth, J. Fierstein, Katmai volcanic cluster and the great eruption of 1912. *Geophys. J. Int*. **112**, 446-453 (2000).

42. B. C. Bautista, M. L. P. Bautista, R. S. Stein, E. S. Barcelona, R. S. Punongbayan, E. P. Laguerta, A. R. Rasdas, G. Ambubuyog, E. Q. Amin, "Relationship of regional and local structures to Mount Pinatubo activity" in *Fire and Mud: Eruptions and Lahars of Mount Pinatubo, Philippines. PHIVOLCS*, C. G. Newhall, R. S. Punongbayan, Eds. (University of Washington Press, Quezon City, 1996), pp. 351-370.

43. J. Mori, R. A. White, D. H. Harlow, P. Okubo, J. A. Power, R. P. Hoblitt, E. P. Laguerta, A. Lanuza, B. C. Bautista, "Volcanic earth quakes following the 1991 climactic eruption of Mount Pinatubo: strong seismicity during a waning eruption" in *Fire and Mud: Eruptions and Lahars of Mount Pinatubo, Philippines. PHIVOLCS*. C. G. Newhall, R. S. Punongbayan, Eds. (University of Washington Press, Quezon City, 1996), pp. 339-350.

44. L. Michon, T. Staudacher, V. Ferrazzini, P. Bachèlery, J. Marti, April 2007 collapse of Piton de la Fournaise: a new example of caldera formation. *Geophys. Res. Lett*., **34**(21) (2007).

45. F. R. Fontaine, G. Roult, L. Michon, G. Barruol, A. Di Muro, The 2007 eruptions and caldera collapse of the Piton de la Fournaise volcano (La Reunion Island) from tilt analysis at a single very broadband seismic station. *Geophys. Res. Lett*. **41**, 2803-2811 (2014); published online EpubApr 28 (10.1002/2014GL059691).

46. A. Di Muro, N. Metrich, D. Vergani, M. Rosi, P. Armienti, T. Fougeroux, E. Deloule, I. Arienzo, L. Civetta, The Shallow Plumbing System of Piton de la Fournaise Volcano (La R,union Island, Indian Ocean) Revealed by the Major 2007 Caldera-Forming Eruption. *J. Petrol*. **55**, 1287-1315 (2014); published online EpubJul (10.1093/petrology/egu025).

47. T. Kaneko, A. Yasuda, T. Shimano, S. Nakada, T. Fujii, T. Kanazawa, A. Nishizawa, Y. Matsumoto, Submarine flank eruption preceding caldera subsidence during the 2000 eruption of Miyakejima Volcano, Japan. *Bull. Volcanol*. **67**, 243-253 (2005); published online EpubMar (10.1007/s00445-004-0407-1).

48. M. Amma-Miyasaka, M. Nakagawa, S. Nakada, Magma plumbing system of the 2000 eruption of Miyakejima Volcano, Japan. *Bull. Volcanol*. **67**, 254-267 (2005); published online EpubMar (10.1007/s00445-004-0408-0).

49. T. Nishimura, S. Ozawa, M. Murakami, T. Sagiya, T. Tada, M. Kaidzu, M. Ukawa, Crustal Deformation caused by magma migration in the northern Izu Islands, Japan. *Geophys. Res. Lett*. **28**, 3745-3748 (2001); published online EpubOct 1 (Doi 10.1029/2001gl013051).

50. S. A. Fedotov, L. B. Slavina, S. L. Senyukov, M. S. Kuchay, Seismic processes and migration of magma during the Great Tolbachik Fissure Eruption of 1975-1976 and Tolbachik Fissure Eruption of 2012-2013, Kamchatka Peninsula. *Izv. Atmos. Ocean Phy*. **51**, 667-687 (2015); published online EpubDec (10.1134/S000143381507004x).

51. S. A. Fedotov, I. S. Utkin, L. I. Utkina, The Peripheral Magma Chamber of Ploskii Tolbachik, a Kamchatka Basaltic Volcano: Activity, Location and Depth, Dimensions, and their Changes Based on Magma Discharge Observations. *J. Volcanol. Seismol*. **5**, 369-385 (2011); published online EpubDec (10.1134/S0742046311060042).

52. P. Doubik, B. E. Hill, Magmatic and hydromagmatic conduit development during the 1975 Tolbachik Eruption, Kamchatka, with implications for hazards assessment at Yucca Mountain, NV. *J. Volcanol. Geotherm. Res*. **91**, 43-64 (1999); published online EpubJul (Doi 10.1016/S0377-0273(99)00052-9).

53. S.A. Fedotov, A. M. Chirkov, N.A. Gusev,G. N. Kovalev, Y. B. Slezin, The large fissure eruption in the region of Plosky Tolbachik volcano in Kamchatka, 1975–1976. *Bull. Volcanol*. **43,** 47-60 (1980).

54. J. Filson, T. Simkin, L. K. Leu, Seismicity of a caldera collapse: Galapagos Islands 1968. J. Geophys. Res., **78**(35), 8591-8622 (1973).

55. J. E. Hammer, M. J. Rutherford, W. Hildreth, Magma storage prior to the 1912 eruption at Novarupta, Alaska. *Contrib. Mineral. Petr*. **144**, 144-162 (2002); published online EpubNov (10.1007/s00410-002-0393-2).

56. M. J. Rutherford, J. D. Devine, in *Fire and Mud: Eruptions and Lahars of Mount Pinatubo, Philippines* C. G. Newhall, R. S. Punongbayan, Eds. (Philippine Institute of Volcanology and Seismology & University of Washington Press, Quezon City, Seattle & London, 1996), pp. 751–766.

57. H. Kanamori, J. Mori, E. Hauksson, T. H. Heaton, L. K. Hutton, L. M. Jones, Determination of earthquake energy release and ML using TERRAscope. Bull. . Seismol. Soc. Am., **83**(2), 330-346 (1993).

58. M. Kikuchi, Y. Yamanaka, K. Koketsu, Source Process of the Long-period Seismic Pulses Associated with the 2000 Eruption of Miyakejima Volcano and its Implications. J. Geograph. Tokyo **110**(2), 204-216 (2001).

References in Supplementary Materials:

59. M. T. Gudmundsson, T. Hognadottir, A. B. Kristinsson, S. Gudbjornsson, Geothermal activity in the subglacial Katla caldera, Iceland 1999-2005, studied with radar altimetry. *Ann. Glacio*. **45**, 66-72 (2007).

60. C. Mätzler, Microwave permittivity of dry snow. *IEEE Trans. Geosci. Remote Sens*. **34**, 573-581 (1996).

61. C. Rossi, C. Minet, T. Fritz, M. Eineder, R. Bamler, Temporal monitoring of subglacial volcanoes with TanDEM-X—Application to the 2014–2015 eruption within the Bárðarbunga volcanic system, Iceland. Remote Sens. Environ. 181, 186-197 (2016)

62. T. Johannesson, H. Björnsson, E. Magnússon, S. Guðmundsson, F. Pálsson, O. Sigurðsson, T. Thorsteinsson, E. Berthier, Ice-volume changes, bias estimation of mass-balance measurements and changes in subglacial lakes derived by lidar mapping of the surface of Icelandic glaciers. *Ann. Glacio.* **54**, 63-74 (2013).

63. E. Magnusson, F. Palsson, H. Bjornsson, S. Gudmundsson, Removing the ice cap of Oraefajokull central volcano, SE-Iceland: Mapping and interpretation of bedrock topography, ice volumes, subglacial troughs and implications for hazards assessments. *Jokull* **62**, 131-150 (2012).

64. H. Bjornsson, F. Pálsson, M. T. Gudmundsson, *Vatnajokull, Northwest Part, 1:100 000: Bedrock topography*, Landsvirkjun and Science Institute, University of Iceland, 1992.

65. A. H. Jarosch, Icetools: A full Stokes finite element model for glaciers. *Comput. Geosci*. **34**, 1004-1014 (2008).

66. J. W. Glen, The Creep of Polycrystalline Ice. *P. Roy. Soc. A-Math. Phy*. **228**, 519-538 (1955).

67. K. M. Cuffey, W. S. B. Paterson, *The Physics of Glaciers.* (Elsevier Butterworth-Heinemann, Burlington, ed. 4, 2010).

68. C. E. Lesher, F. J. Spera, "Thermodynamic and Transport Properties of Silicate Melts and Magma" in *The Encyclopedia of Volcanoes*, H. Sigurdsson, B. Houghton, H. Rymer, Eds. (Academic Press, Academic Press, Heidelberg, Amsterdam, Boston, ed. 2, 2015), pp. 113-141.

69. R. Bödvarsson, S. T. Rögnvaldsson, R. Slunga, E. Kjartansson, The SIL data acquisition system—at present and beyond year 2000. *Phys. Earth Planet. Inter*. **113**, 89-101 (1999).

70. R. Slunga, S. T. Rögnvaldsson, R. Bödvarsson, Absolute and relative locations of similar events with application to microearthquakes in southern Iceland. *Geophys. J. Int*. **123**, 409–419 (1995).

71. S. Th. Rögnvaldsson, R. Slunga, Routine fault plane solutions for local networks: a test with synthetic data. Bull. Seism. Soc. Am. **83**.4, 1232-1247 (1993).

72. R. Stefánsson, R. Böđvarsson, R. Slunga, P. Einarsson, S. Jakobsdóttir, H. Bungum, S. Gregersen, J. Havskov, J. Hjelme, H. Korhonen, Earthquake prediction research in the South Iceland seismic zone and the SIL project. *Bull. Seism. Soc. Am*. **83**, 696–716 (1993).

73. S., A., R. Cesca, T. Dahm, Discrimination of induced seismicity by full moment tensor inversion and decomposition. *J. Seimsol*. **17**, 147-163 (2013).

74. P. A. Rosen, S. Hensley, I. R. Joughin, F. K. Li, S. N. Madsen, E. Rodriguez, R. M. Goldstein, Synthetic aperture radar interferometry, presented at *Proceedings of the IEEE*, 2000 (unpublished).

75. B. Kampes, Delft Object-oriented Radar Interferometric Software: User's Manual and Technical Documentation v4.02, presented at *Delft Technical University*, 1999 (unpublished).

76. Y. Y. Kagan, 3-D rotation of double-couple earthquake sources. *Geophys. J. Int*. **106**, 709–716 (1991).

77. R. M. Goldstein, C. L. Werner, Radar interferogram filtering for geophysical applications. *Geophys. Res. Lett*. **25**, 4035-4038 (1998).

78. C. W. Chen, H. A. Zebker, Two-dimensional phase unwrapping with use of statistical models for cost functions in nonlinear optimization. *J. Opt. Soc. Am. A Opt. Image. Sci. Vis.* **18**, 338-351 (2001).

79. Y. Okada, Internal deformation due to shear and tensile faults in a half-space. *B. Seismol. Soc. Am*. **82**, 1018-1040 (1992).

80. A. Hooper, J. Pietrzak, W. Simons, H. Cui, R. Riva, M. Naeije, A. Terwisscha van Scheltinga, E. Schrama, G. Stelling, A. Socquet, Importance of horizontal seafloor motion on tsunami height for the 2011 Mw=9.0 Tohoku-Oki earthquake. *Earth Planet. Sc. Lett*. **361**, 469-479 (2013).

81. C. E. Ford, D. G. Russell, J. A. Craven, M. R. Fisk, Olivine-liquid equilibria: Temperature, pressure and composition dependence of the crystal/liquid cation partition coefficients for Mg, Fe2+, Ca and Mn. *J. Petrol.* **24**, 256-266 (1983).

82. H. J. Yang, R. J. Kinzler, T. L. Grove, Experiments and models of anhydrous, basaltic olivine-plagioclase-augite saturated melts from 0.001 to 10 kbar. *Contrib. Mineral. Petr*. **124**, 1-18 (1996).

83. G. H. Gudfinnsson, D. C. Presnall, A pressure-independent geothermometer for primitive mantle melts. *J. Geophys. Res*. **106**, B8 (2001).

84. K. D. Putirka, Thermometers and barometers for volcanic systems. *Rev. Mineral. Geochem*. **69**, 61-120 (2008).

85. Y. Kawakami, J. Yamamoto, H. Kagi, Microraman densimeter for CO2 inclusions in mantle derived minerals. *Appl. Spectrosc*. **57**, 1333-1339 (2003).

86. M.R. Burton, P. Allard, F. Mure, A. La Spina, Magmatic gas composition reveals the source depth of slug-driven Strombolian explosive activity, *Science*, **317**, 5835, 227-230 (2007), doi:10.1126/science.1141900.

87. A. Aiuppa, C. Federico, G. Giudice, S. Gurrieri, Chemical mapping of a fumarolic field: La Fossa Crater, Vulcano Island (Aeolian Islands, Italy), *Geophys. Res. Lett.*, **32** (13) (2005), p. L13309 http://dx.doi.org/10.1029/2005GL023207

88. P.-J. Gauthier, O. Sigmarsson, M. Gouhier, B. Haddadi, and S. Moune, Elevated gas flux and trace metal degassing from the 2014–2015 fissure eruption at the Bárðarbunga volcanic system, Iceland, *J. Geophys. Res. Solid Earth*, **121**, (2016) doi:10.1002/2015JB012111.

89. E. Bali, O. Sigmarsson, S. Jakobsson, H. Gunnarsson, Volatile budget of the Nornahraun eruption in the Bárðarbunga system, Iceland. Geophysical Research Abstracts Vol. 17, EGU2015-5757, 2015 EGU General Assembly (2015). http://meetingorganizer.copernicus.org/EGU2015/EGU2015-5757.pdf

90. A. Burgisser, M. Alletti, B. Scaillet, Simulating the behavior of volatiles belonging to the C–O–H–S system in silicate melts under magmatic conditions with the software D-Compress, *Comput. Geosci.*, **79**, 1–14.

91. D. O. Potyondy, P. A. Cundall, A bonded particle model for rock. *Int. J. Rock Mech. Min.* **41**, 1329-1364 (2004).

92. D. Mas Ivars, M. E. Pierce, C. Darcel, J. Reyes-Montes, D. O. Potyondy, R. P. Young, P. A. Cundall, The synthetic rock mass approach for jointed rock mass modelling. *Int. J. Rock Mech. Min*. **48**, 219-244 (2011).

93. Itasca Consulting Group, Inc. *PFC2D - Particle Flow Code in Two-Dimensions*, *Ver. 5.0.* Minneapolis, Itasca (2014).

94. K. Mogi, Relations between the eruptions of various volcanoes and the deformations of the ground surfaces around them. *B. Earthq. Res. Inst. Univ. Tokyo* **36**, 99–134 (1958).

95. M. Ripepe, D. Delle Donne, R. Genco, G. Maggio, M. Pistolesi, E. Marchetti, G. Lacanna, G. U. P. Poggi, Volcano seismicity and ground deformation unveil the gravity-driven magma discharge dynamics of a volcanic eruption. *Nat. Commun*. **6** (2015).

96. Y. Bottinga, D. Weill, The viscosity of magmatic silicate liquids: a model for calculation. *Am. J. Sci*. **272**, 438–475 (1972).

Acknowledgements

A large part of the field effort was supported with crisis response funding from the Icelandic Government through the Civil Protection Department of the National Commissioner of the Icelandic Police. A considerable part of this work was made possible through the European Community‘s Seventh Framework Programme Grant No. 308377 (Project FUTUREVOLC). Further support came from the EU Seventh Framework Marie Curie project NEMOH No. 289976, and the project CO2Volc ERC grant No. 279802, the Research Fund of the University of Iceland, the Irish Research Council, the Helmholtz Alliance on Remote Sensing and Earth System Dynamics (EDA) and UNAM/CIC Intercambio Académico. We thank the following key persons for help with instrumentation and data: B.H. Bergsson, V.S. Kjartansson, S. Steinthorsson, Th. Jónsson, P. Erlendsson, J. Soring, I. Jónsdóttir, G. Sverrisdóttir and G. Sigurdsson, the SIL network monitoring team at the IMO, the field observation team of the IES in Holuhraun, and for collaboration on seismic instruments and data we thank R.S. White and the Cambridge team and C. Bean and the UCD team. The subsidence of Bárðarbunga was mapped by the surveying aircraft of Isavia (Icelandic Aviation Operation Services) and from satellite images acquired by Pléiades (Centre National d'Études Spatiales (CNES) CNES 2014, Distributed Airbus DS, subsidized access provided by the French Space Agency CNES’s ISIS programme) and SPOT 6 (©Airbus DS 2014). Committee on Earth Observation Satellites (CEOS) and Geohazards Supersites and Natural Laboratories (GSNL) also provided access to satellite data. COSMO-SkyMed data were provided by the Italian Space Agency (ASI) through the Iceland Volcanoes Supersite agreement. The Icelandic Coast Guard provided valuable aeroplane and helicopter support for the field effort. Field operations at Bárdarbunga were supported by the Landsvirkjun power company, the Iceland Glaciological Society and Vatnajökull National Park.

One page summary:

Gradual caldera collapse at Bárdarbunga volcano, Iceland, regulated by lateral magma outflow

Magnús T. Gudmundsson[1], Kristín Jónsdóttir[2], Andrew Hooper[3], Eoghan P. Holohan[4,5], Saemundur A. Halldórsson[1], Benedikt G. Ófeigsson[2], Simone Cesca[4], Kristín S. Vogfjörd[2], Freysteinn Sigmundsson[1], Thórdís Högnadóttir[1], Páll Einarsson[1], Olgeir Sigmarsson[1,6], Alexander H. Jarosch[1], Kristján Jónasson[7], Eyjólfur Magnússon[1], Sigrún Hreinsdóttir[8], Marco Bagnardi[3], Michelle M. Parks[1], Vala Hjörleifsdóttir[9], Finnur Pálsson[1], Thomas R. Walter[4], Martin P.J. Schöpfer[10], Sebastian Heimann[4], Hannah I. Reynolds[1], Stéphanie Dumont[1], Eniko Bali[1], Gudmundur H. Gudfinnsson[1], Torsten Dahm[4], Matthew Roberts[2], Martin Hensch[2], Joaquín, M.C. Belart[1], Karsten Spaans[3], Sigurdur Jakobsson[1], Gunnar B. Gudmundsson[2], Hildur M. Fridriksdóttir[1,2], Vincent Drouin[1], Tobias Dürig[1], Gudfinna Adalgeirsdóttir[1], Morten S. Riishuus[1], Gro B.M. Pedersen[1], Tayo van Boeckel[1] , Björn Oddsson[11], Melissa A. Pfeffer[2], Sara Barsotti[2], Baldur Bergsson[2], Amy Donovan[12], Mike R. Burton[13], Alessandro Aiuppa[14]

INTRODUCTION: The Bárdarbunga caldera volcano in central Iceland collapsed from August 2014 – February 2015 during the largest eruption in Europe since 1784. An ice-filled subsidence bowl 8 x11 km wide and up to 65 m deep developed, while magma drained laterally for 45 km along a subterranean path and erupted as a major lava flow northeast of the volcano. Our data provide unprecedented insight into of the workings of a collapsing caldera.

RATIONALE: Collapses of caldera volcanoes are, fortunately, not very frequent, as they are often associated with very large volcanic eruptions. On the other hand, the rarity of caldera collapses limits insight into this major geological hazard. Since the formation of Katmai caldera in 1912, during the 20th century's largest eruption, only five caldera collapses are known to have occurred before that at Bárdarbunga. We used aircraft-based altimetry, satellite photogrammetry, radar interferometry, ground-based GPS, evolution of seismicity, radio-echo soundings of ice thickness, ice flow modeling and geobarometry to describe and analyze the evolving subsidence geometry, its underlying cause, the amount of magma erupted, the geometry of the subsurface caldera ring faults and the moment tensor solutions of the collapse-related earthquakes.

RESULTS: After initial lateral withdrawal of magma for some days though a magma-filled fracture propagating through the Earth's upper crust, pre-existing ring faults under the volcano were reactivated over the period 20-24 August, marking the onset of collapse. On August 31, the eruption started and it terminated when the collapse stopped, having produced 1.5 km^3 of basaltic lava. The subsidence of the caldera declined with time in a near exponential manner, in phase with the lava flow rate.

The volume of the subsidence bowl was about 1.8 km^3. Using radio-echo soundings, we find that the subglacial bedrock surface after the collapse is down-sagged with no indications of steep fault escarpments. Using geobarometry, we determined the source depth of the magma to be approximately 12 km and modelling of geodetic observations gives a similar result. High precision earthquake locations and moment tensor analysis of the remarkable magnitude M5 earthquake series are consistent with steeply dipping ring faults. Statistical analysis of seismicity reveals communication over tens of kilometers between the caldera and the dyke.

CONCLUSIONS: We conclude that interaction between the pressure exerted by the subsiding reservoir roof and the physical properties of the subsurface flow path explain the gradual near exponential decline of both collapse rate and the intensity of the 181-day long eruption. By combining our various data sets, we show that the onset of collapse was caused by outflow of

magma from underneath the caldera when 12-20% of the total magma intruded and erupted had flowed from the magma reservoir. However, the continued subsidence was driven by a feedback between the pressure of the piston-like block overlying the reservoir, and the 47 km long magma outflow path. Our data provide better constraints on caldera mechanisms than previously available, demonstrating what caused the onset, and how both the roof overburden and the flow path properties regulate the collapse.

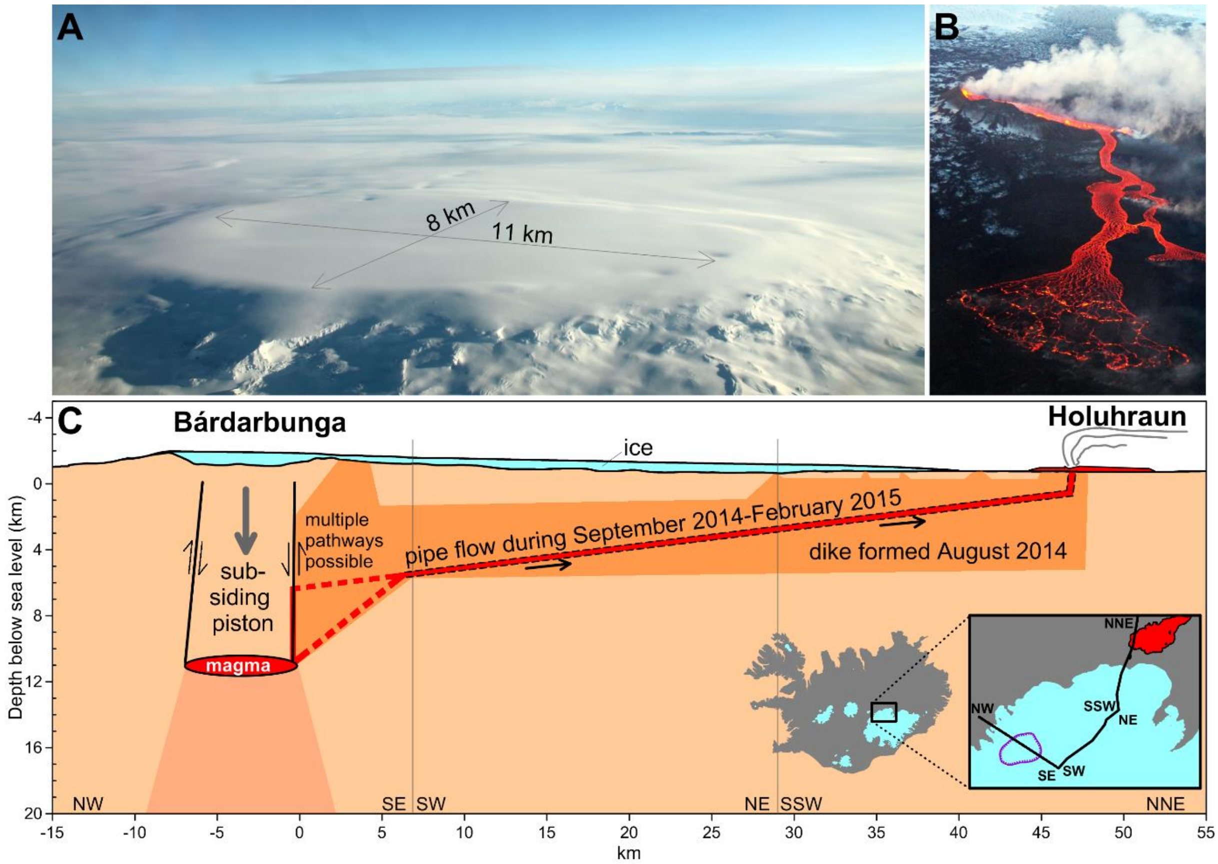

The Bárdarbunga caldera and the lateral magma flowpath to the Holuhraun eruption site. (**A**) Aerial view of the ice-filled Bárdarbunga caldera on 24 October 2014, view from the north. (**B**) The effusive eruption in Holuhraun, 45 km to the northeast of the caldera. (**C**) A schematic cross-section through the caldera and along the lateral subterranean flow path between the magma reservoir and the surface.